

UCSB-HEP-94-05
 DTP/94/12
 UCD-94-8
 May 1994

Three-jet final states and measuring the $\gamma\gamma$ width of the Higgs at a photon linear collider

D. L. Borden

*Department of Physics, University of California
 Santa Barbara, California 93106, USA*

and

V. A. Khoze and W. J. Stirling

*Department of Physics, University of Durham
 Durham DH1 3LE, England*

and

J. Ohnemus

*Department of Physics, University of California
 Davis, California 95616, USA*

Abstract

The identification of the intermediate-mass Higgs process $\gamma\gamma \rightarrow H \rightarrow b\bar{b}$ will be one of the most important goals of a future photon linear collider. Potentially important backgrounds from the continuum $\gamma\gamma \rightarrow c\bar{c}, b\bar{b}$ leading-order processes can be suppressed by a factor m_q^2/s by using polarized photon beams in the $J_z = 0$ initial-state configuration. We show that the same m_q^2/s suppressions do not necessarily apply to the radiative processes $\gamma\gamma \rightarrow c\bar{c}g, b\bar{b}g$. These processes can mimic the two-jet topology of the Higgs signal when two of the three partons are collinear, or when one of the partons is soft or directed down the beam pipe. We calculate the contribution of these processes to the two-jet background in the $J_z = 0$ channel. The largest background is from the $\gamma\gamma \rightarrow c\bar{c}g \rightarrow 2$ jets process, which yields a cross section in excess of the Higgs signal. We investigate the effect of imposing additional event shape, jet width and secondary vertex cuts on both signal and background, and show that with reasonable detector capabilities it should be possible to reduce the background to a manageable level.

1 Introduction

The rapid advance of laser technology makes possible the collision of high-brightness, high-energy photon beams at future linear colliders [1, 2, 3] through Compton backscattering [4, 5]. One particularly intriguing use of such a photon linear collider is to measure the two-photon decay width of a Higgs boson once it is discovered [6, 7]. The $\gamma\gamma$ width of a Higgs boson is potentially one of its most important properties. The coupling of the Higgs to two photons proceeds through loops in which any charged particle with couplings to the Higgs contributes. A measurement of the $\gamma\gamma$ width is thus quite sensitive to new physics at even higher mass scales [6]. Supersymmetric models, technicolor models, and other extensions of the standard model with more complicated Higgs sectors all predict two-photon couplings which are, in general, very different from that of the standard model [8, 9].

In a photon linear collider, the $\gamma\gamma$ partial width of a Higgs boson, $\Gamma(H \rightarrow \gamma\gamma)$, is deduced by measuring the Higgs production cross section in the reaction $\gamma\gamma \rightarrow H \rightarrow X$ where X is the detected final state. The number of detected events is proportional to the product $\Gamma(H \rightarrow \gamma\gamma) B(H \rightarrow X)$ where $B(H \rightarrow X)$ is the branching ratio of the Higgs boson into the detected final state X . Measuring the production cross section then determines this product. An independent measurement of the branching ratio, say at an e^+e^- collider in the process $e^+e^- \rightarrow ZH \rightarrow ZX$, then allows a determination of the $\gamma\gamma$ partial width.

For a Higgs boson in the intermediate-mass region, $50 \text{ GeV} \lesssim M_H \lesssim 150 \text{ GeV}$, the dominant decay mode is to $b\bar{b}$. Measurement of the two-photon partial width of the Higgs in this mass region requires suppressing the continuum $\gamma\gamma \rightarrow b\bar{b}, c\bar{c}$ background beneath the resonant $\gamma\gamma \rightarrow H \rightarrow b\bar{b}$ signal, assuming light quarks can be distinguished from heavy quarks by vertexing [7]. The continuum background can be greatly suppressed by using polarized photon beams. The Higgs signal is produced by photons in a $J_z = 0$ initial state, whereas the continuum backgrounds are primarily produced by photons in the $J_z = \pm 2$ initial state, the $J_z = 0$ cross section being suppressed for large angles by a factor of m_q^2/s [6, 10].

It is important to note that the m_q^2/s suppression of the $J_z = 0$ $\gamma\gamma \rightarrow q\bar{q}$ cross section is in principle removed by the presence of an additional gluon in the final state. It follows that $\gamma\gamma \rightarrow q\bar{q}g$ with $q = b, c$ could be a significant background for Higgs detection. This process can mimic a two-jet event (the dominant signal topology) in two important ways: (i) if two of the three partons are collinear, for example a fast quark recoiling against a collinear quark and gluon, or (ii) if one of the three partons is either quite soft or is directed down the beampipe and is therefore not tagged as a distinct jet. A particularly interesting example of the latter is when one of the incoming photons splits into a quark and an antiquark, one of which carries most of the photon's momentum and Compton scatters off the other photon, $q(\bar{q})\gamma \rightarrow q(\bar{q})g$. Two jets are then identified in the detector, with the third jet remaining undetected.

In this paper we study the impact of the radiative $q\bar{q}g$ production process on the study of an intermediate-mass Higgs boson at a photon linear collider. We first describe the calculation of the matrix element and discuss the various configurations which could be tagged as two-jet events. In Section 3, we perform a detailed experimental simulation and

compare the resulting background cross sections with those expected from Higgs production. Finally, our conclusions are presented in Section 4.

2 Matrix Elements and Cross Sections

2.1 Higgs Production

For Higgs bosons in the intermediate-mass region, the beam energy spread of a $\gamma\gamma$ collider is much greater than the total width of the Higgs boson, and so the number of $H \rightarrow b\bar{b}$ events expected is

$$N_{H \rightarrow b\bar{b}} = \frac{dL_{\gamma\gamma}^{J_z=0}}{dW_{\gamma\gamma}} \Big|_{M_H} \frac{8\pi^2 \Gamma(H \rightarrow \gamma\gamma) B(H \rightarrow b\bar{b})}{M_H^2} \quad (1)$$

where $W_{\gamma\gamma}$ is the two-photon invariant mass. Figure 1 shows the production rate for $\gamma\gamma \rightarrow H \rightarrow b\bar{b}$ events in the standard model with a typical value of $0.2 \text{ fb}^{-1}/\text{GeV}$ taken for dL/dW . The width and branching ratio are taken from Ref. [8] and a top quark mass of 150 GeV is assumed.

2.2 Non-radiative background

The non-radiative ($\gamma\gamma \rightarrow b\bar{b}, c\bar{c}$) continuum background cross section is given by

$$\begin{aligned} \frac{d\sigma(\gamma\gamma \rightarrow q\bar{q})}{d\cos\theta} &= \frac{12\pi\alpha^2 Q_q^4}{s} \frac{\beta}{(1 - \beta^2 \cos^2\theta)^2} \\ &\times \begin{cases} 1 - \beta^4 & \text{for } J_z = 0 \\ \beta^2(1 - \cos^2\theta)(2 - \beta^2 + \beta^2 \cos^2\theta) & \text{for } J_z = \pm 2 \end{cases} \end{aligned} \quad (2)$$

where $\beta \equiv \sqrt{1 - 4m_q^2/s}$ is the velocity of the outgoing quarks, and m_q and Q_q are the mass and fractional electric charge of the quark respectively. The $\gamma\gamma$ center-of-mass collision energy is $W_{\gamma\gamma} = \sqrt{s}$. Note the strong $\cos\theta$ dependence of the cross section and that the $J_z = 0$ cross section vanishes, for $|\cos\theta| < 1$, in the high-energy ($\beta \rightarrow 1$) limit. This background can therefore be significantly reduced by using polarized beams and cutting on $\cos\theta$.

Direct comparison of the continuum background cross sections with the resonant signal cross section is difficult. As indicated in Eq. (1), the event rate of signal events is proportional to dL/dW while the event rate for the continuum background is proportional to the total luminosity; comparing the two requires choosing a suitable integration range for W . In comparing signal (S) to background (B) cross sections, we have chosen to normalize the signal cross sections as if $(dL/dW)_S = (L)_B/(10 \text{ GeV})$. This is equivalent, for the purposes of comparison, to assuming that the experimental resolution on reconstructing the Higgs mass is 10 GeV.

Figure 2 shows two-photon cross sections for $b\bar{b}$ and $c\bar{c}$ production in polarized collisions and demonstrates the very large suppression that is possible with polarized photons in the $J_z = 0$ state. A cut of $|\cos \theta| < 0.7$ has been applied. For comparison, the Higgs boson signal has been superimposed, with the normalization as described in the previous paragraph. It is clear that a high degree of polarization will be crucial in suppressing these continuum backgrounds below the Higgs signal.

Before discussing the radiative background we comment briefly on the origin of the large-angle suppression of $q\bar{q}$ production in the $J_z = 0$ channel as $m_q^2/s \rightarrow 0$. Consider the symmetry properties of the Born amplitude in the $\beta \rightarrow 1$ limit. Because of helicity conservation at the photon vertices, only amplitudes with opposite helicities for the quark and antiquark survive. However, the combined impact of C -, P - and T -invariance, photon Bose statistics, and unitarity, can be shown to lead to a vanishing amplitude in this limit *at lowest order in perturbation theory*. It follows that all interferences between the Born and higher-order non-radiative diagrams also vanish for the $J_z = 0$ case. In fact for the special case of scattering at angle $\theta = 90^\circ$, the vanishing of *all* $J_z = 0$ non-radiative amplitudes (i.e. not just at leading order) follows simply from rotational invariance about the fermion direction and photon Bose statistics. For this particular angular configuration the T -invariance argument is redundant.

2.3 Radiative background

The non-radiative backgrounds discussed above were considered in Ref. [7] with regard to Higgs physics in $\gamma\gamma$ collisions. With highly polarized beams, such backgrounds are found to be small and do not hinder the study of an intermediate-mass Higgs boson at a $\gamma\gamma$ collider. This raises the question of whether previously ignored backgrounds could in fact be dominant, or at least could contribute significantly.

While the lowest order $q\bar{q}$ large-angle cross sections are $\mathcal{O}(\alpha^2/s)$ and $\mathcal{O}(\alpha^2 m_q^2/s^2)$ for $J_z = \pm 2$ and 0, respectively, the $q\bar{q}g$ cross sections are $\mathcal{O}(\alpha^2 \alpha_s/s)$ in both cases, i.e. the $\gamma\gamma \rightarrow q\bar{q}g$ cross section is in principle *not* suppressed in the $J_z = 0$ channel at high energies as is the non-radiative cross section. Furthermore, as we shall see below, there are regions of phase space where the three-parton final state may be tagged as a two-jet event. In the case of $b\bar{b}g$ and $c\bar{c}g$, the event may have a vertex structure similar to the non-radiative case, in which case this process could easily be misidentified as a $b\bar{b}$ final state. In contrast, the $J_z = \pm 2$ cross section for $\gamma\gamma \rightarrow q\bar{q}g$ is simply an $\mathcal{O}(\alpha_s)$ correction to the much larger $J_z = \pm 2$ $\gamma\gamma \rightarrow q\bar{q}$ cross section and will not be considered further here.

The full matrix element squared for $\gamma\gamma \rightarrow q\bar{q}g$ with massive quarks is too long to write down here, but the matrix element with massless quarks is particularly simple and contains most of the important physics. As a first step, we examine the massless cross section in detail, reserving the consideration of the massive case until later. In all that follows (both massless and massive cross sections) the following labelling conventions are adopted:

$$\gamma(\lambda_1, k_1) + \gamma(\lambda_2, k_2) \rightarrow q(p) + \bar{q}(\bar{p}) + g(k), \quad (3)$$

where the λ_i 's are the photon helicities and the k 's and p 's are the particle four-momenta.

2.3.1 Massless Quarks

In the limit of vanishing quark masses, the $J_z = 0$ ($\lambda_1 = \lambda_2$) matrix element squared for $\gamma\gamma \rightarrow q\bar{q}g$ is given by [11]

$$\left|M_{J_z=0}(\gamma\gamma \rightarrow q\bar{q}g)\right|^2 = 32 g_s^2 e^4 Q_q^4 \frac{(p \cdot \bar{p}) [(p \cdot k)^2 + (\bar{p} \cdot k)^2]}{(p \cdot k_1)(p \cdot k_2)(\bar{p} \cdot k_1)(\bar{p} \cdot k_2)}. \quad (4)$$

It is instructive to write the cross section in terms of the quark and antiquark energies. Note that the final-state parton kinematics are fully specified by these two energies and three Euler angles which give the orientation of the final state with respect to the initial state. Defining

$$x \equiv 2 p_0 / \sqrt{s}, \quad \bar{x} \equiv 2 \bar{p}_0 / \sqrt{s}, \quad \cos \theta \equiv p_z / p_0, \quad \cos \bar{\theta} \equiv \bar{p}_z / \bar{p}_0, \quad (5)$$

the cross section is given by

$$\begin{aligned} d\sigma_{J_z=0}(\gamma\gamma \rightarrow q\bar{q}g) &= \frac{16 \alpha_s \alpha^2 Q_q^4}{\pi^2 s} \frac{(x + \bar{x} - 1)[(1 - x)^2 + (1 - \bar{x})^2]}{x^2 \bar{x}^2} \\ &\times \frac{dx d\bar{x} d\alpha d\cos \beta d\gamma}{(1 - \cos^2 \theta)(1 - \cos^2 \bar{\theta})}, \end{aligned} \quad (6)$$

where α , β , and γ are the Euler angles.

Although at the parton level this process results in a three-particle final state, in practice the event topology following fragmentation and hadronization may appear to be two-jet-like. This can occur in two distinct ways: two of the three partons may be collinear and so will appear as a single jet [see Fig. 3(a)]; or one of the partons may be soft or may be directed down the beampipe and so not recognized as a distinct jet [see Fig. 3(b)].

In the approximation that the detector covers 4π of solid angle, the two- versus three-jet nature of the cross section is independent of the orientation of the final state and so depends only on x and \bar{x} . The cross section is defined over the Dalitz-plot triangle in $x-\bar{x}$ space shown in Fig. 4. In general, the two-jet-like region corresponds to the periphery of the triangle while the three-jet-like events are confined to the interior. In the two-jet region, the collinear regime corresponds to the edges of the triangle while the soft-parton regime corresponds to the corners. Note that the $(x \approx 1, \bar{x} \approx 1)$ corner of the triangle is the region of soft gluon emission. In this corner the quark and antiquark are energetic and back-to-back, with the gluon being quite soft. The $q\bar{q}g$ cross section is highly suppressed here; in fact, the differential cross section behaves as $d\sigma/dE_g \sim E_g^3$.¹ This is in marked contrast to the $J_z = \pm 2$ case, where the cross section exhibits the standard infrared behaviour $d\sigma/dE_g \sim E_g^{-1}$. In the other corners of the triangle, $(x \approx 1, \bar{x} \approx 0)$ and $(x \approx 0, \bar{x} \approx 1)$, it is one of the quarks which is soft.

¹The physical origin of this behaviour can be understood by recalling the celebrated Low expansion [12] of the matrix element in powers of E_g , extended to the case of charged fermions by Burnett and Kroll [13].

Discriminating two- from three-jet topologies on an event-by-event basis requires specifying a jet-finding algorithm. A convenient formalism to use is a clustering formalism, exemplified by the JADE algorithm [14]. In such a scheme, particle pairs with low invariant mass are iteratively combined into one particle (by adding their four-momenta) until no remaining pair has squared invariant mass below some cutoff. In general, the cutoff is specified as a fraction of the total event invariant mass squared and is traditionally called y_{cut} . Pure $q\bar{q}$ events are efficiently tagged with a y_{cut} of 0.02–0.03.

2.3.2 Collinear regime

If the JADE algorithm is applied at the parton level to the $\gamma\gamma \rightarrow q\bar{q}g$ process, some simple approximations allow an analytic expression for the two-jet cross section as a function of y_{cut} . If $y_{\text{cut}} \ll 1$, the region of integration is confined to the very edges of the x, \bar{x} triangle, where one parton takes nearly half the event energy and the other two partons are collinear and recoil against it. Assuming that all three parton momenta are nearly collinear allows the cross section to be integrated analytically. Taking the resulting two final-state jets to lie in the central region of the detector, with $|\cos\theta_{\text{thrust}}| < \cos\theta_0$, the $\gamma\gamma \rightarrow q\bar{q}g \rightarrow 2$ jet cross section is given by:

$$\begin{aligned}\sigma(q\bar{q}g \rightarrow 2 \text{ jets}) &= \frac{128 \alpha_s \alpha^2 Q_q^4}{s} F_1(\cos\theta_0) G(y_{\text{cut}}), \\ F_1(z) &= \frac{1}{4} \ln\left(\frac{1+z}{1-z}\right) + \frac{z}{2(1-z^2)}, \\ G(y) &= 7 - \frac{2}{3}\pi^2 + \left[\frac{2y(y^3 + 3y^2 - 11y - 9)}{(1+y)^2(1-y)} + 4 \ln\left(\frac{1+y}{1-y}\right) \right] \ln\left(\frac{2y}{1-y}\right) \\ &\quad + \frac{(3y-1)(y^3 - 5y^2 - y + 7)}{(1+y)(1-y)^2} + 4 \text{Li}_2\left(\frac{1-y}{1+y}\right) - 4 \text{Li}_2\left(\frac{2y}{1+y}\right),\end{aligned}\tag{7}$$

where the dilogarithm function is defined by

$$\text{Li}_2(x) = - \int_0^x \frac{\ln(1-t)}{t} dt = \sum_{n=1}^{\infty} \frac{x^n}{n^2}.\tag{8}$$

Note that when y is small, $G(y) \sim 2y \ln(1/2y) - y$. In particular, for y_{cut} values from 0.01 to 0.1, $G(y_{\text{cut}})$ runs from about 0.07 to 0.3.

Compare Eq. (7) to the non-radiative $J_z = \pm 2$ cross section, given in the massless limit by

$$\begin{aligned}\sigma(q\bar{q}) &= \frac{24\pi \alpha^2 Q_q^4}{s} F_2(\cos\theta_o), \\ F_2(z) &= \ln\left(\frac{1+z}{1-z}\right) - z.\end{aligned}\tag{9}$$

For $\cos\theta_o = 0.7$, F_1 and F_2 are 1.120 and 1.035, respectively. The $J_z = 0$ radiative cross section in this approximation, assuming a y_{cut} and $\cos\theta_0$ of 0.03 and 0.7 respectively, is approximately 3% of the non-radiative $J_z = \pm 2$ cross section.

2.3.3 Compton regime

The $\gamma\gamma \rightarrow q\bar{q}g \rightarrow 2$ jets cross section also receives contributions from configurations where only two of the final state partons appear as jets in the detector. Inspection of Eq. (4) reveals that the matrix element squared can become large when one of the final state quarks is either very soft or is collinear with one of the incoming photons, e.g. $p \cdot k_1 \rightarrow 0$. This important contribution corresponds to one of the photons splitting into a quark and an antiquark, one of which undergoes a hard Compton scattering with the other photon to produce an energetic quark and gluon in the final state [see Fig. 3(b)]. The extent to which these two jets are back-to-back in the $\gamma\gamma$ center-of-mass frame (and therefore constitute a background to $H \rightarrow q\bar{q}$) depends on how the momentum is apportioned between the active and spectator quark in the $\gamma \rightarrow q\bar{q}$ splitting – the more asymmetric the splitting, the more back-to-back are the jets.

To estimate the size of this virtual Compton scattering contribution, we can use the leading pole approximation [15], i.e.

$$d\sigma(\gamma\gamma \rightarrow q\bar{q}g) \simeq d\mathcal{W}(\gamma \rightarrow q\bar{q}) d\sigma(q\gamma \rightarrow qg)|_{p^*=k_1-\bar{p}}, \quad (10)$$

$$d\mathcal{W}(\gamma \rightarrow q\bar{q}) = \frac{\alpha Q_q^2}{4\pi^2} \left[\frac{\bar{x}^2 + (1-\bar{x})^2}{k_1 \cdot \bar{p}} + \frac{(1-\bar{x})m_q^2}{(k_1 \cdot \bar{p})^2} \right] \frac{d^3\bar{p}}{\bar{p}_0}, \quad (11)$$

where $\bar{x} = 2\bar{p}_0/\sqrt{s}$ is the energy fraction of the quark which does not participate in the hard scattering.² For this process to give a two-jet background, most of the $\gamma\gamma$ scattering energy \sqrt{s} should be deposited in the detector, thus $0 < \bar{x} < \epsilon$ where ϵ is a small parameter that will be directly related to the allowed acollinearity of the two jets in the detector. In particular, if we use the JADE algorithm to define the two-jet sample then $\epsilon \sim y_{\text{cut}}$.

The transverse momentum integration of the spectator quark gives rise to a large logarithm, $\sim \ln(\Delta s/m_q^2)$, where Δs is some fraction of s , and so the overall size of this contribution is roughly

$$\sigma(\gamma\gamma \rightarrow q\bar{q}g \rightarrow 2 \text{ jets})_{\text{Compton}} \simeq \frac{\alpha Q_q^2}{2\pi} \mathcal{O}(\epsilon) \ln\left(\frac{\Delta s}{m_q^2}\right) \sigma(q\gamma \rightarrow qg). \quad (12)$$

The form of Eq. (11) is correct for unpolarized scattering, but in fact there is no particularly strong helicity dependence for this contribution. In particular there is no $J_z = 0$ suppression in this case.

Note that the requirement that most of the collision energy should be deposited at large angles in the detector provides a very strong suppression of other ‘resolved photon’ contributions, such as $\gamma \rightarrow gX$ followed by $g\gamma \rightarrow q\bar{q}$. These processes will therefore not be considered further here.

²There are of course analogous contributions with $q \leftrightarrow \bar{q}$ and $k_1 \leftrightarrow k_2$.

To summarize, we have identified two potentially important backgrounds arising from $J_z = 0$ $\gamma\gamma \rightarrow q\bar{q}g$ production. It is instructive to compare these with the leading order background at the level of couplings and small quantities:

$$\sigma(\gamma\gamma \rightarrow q\bar{q})_{\text{LO}} \sim \frac{\alpha^2}{s} \mathcal{O}\left(\frac{m_q^2}{s}\right), \quad (13)$$

$$\sigma(\gamma\gamma \rightarrow q\bar{q}g \rightarrow 2 \text{ jets})_{\text{collinear}} \sim \frac{\alpha^2}{s} \alpha_s \mathcal{O}(y_{\text{cut}} \ln(1/y_{\text{cut}})), \quad (14)$$

$$\sigma(\gamma\gamma \rightarrow q\bar{q}g \rightarrow 2 \text{ jets})_{\text{Compton}} \sim \frac{\alpha^2}{s} \alpha_s \mathcal{O}(y_{\text{cut}}) \ln\left(\frac{\Delta s}{m_q^2}\right). \quad (15)$$

In Section 3, we will present a detailed experimental study of these backgrounds. Before doing so, we discuss how the results change when the quark mass is included in the $q\bar{q}g$ matrix element.

2.3.4 Massive Quarks

The matrix element for $\gamma\gamma \rightarrow q\bar{q}g$ with massive quarks and arbitrary initial state photon helicities λ_1, λ_2 was calculated numerically by both spinor techniques and by direct computation of the four-component amplitude. Examples of calculations using these methods can be found in Refs. [16] and [17]. The numerical results from the two methods agree to better than 1 part in 10^5 . In both methods the matrix elements were checked for invariance under changes of the photon and gluon gauge. Furthermore, in the massless limit ($m_q \rightarrow 0$) the numerical results agree with the results from the analytic expression in Eq. (4). Finally, the matrix elements also reproduce the analytic soft-gluon results for massive quarks.

The main difference between the massive and massless $J_z = 0$ matrix elements is that the massless matrix element is infrared finite, whereas the massive matrix element has an infrared singularity in the limit $k \rightarrow 0$. To illustrate the general features of the $\gamma\gamma \rightarrow q\bar{q}g$ cross sections, we chose $\gamma\gamma$ collisions with center of mass energy $\sqrt{s} = 200$ GeV, $m_b = 4.5$ GeV, and $\alpha = 1/137$. The helicity combination $\lambda_1 = \lambda_2$ ($J_z = 0$) gives the background to $\gamma\gamma \rightarrow H \rightarrow b\bar{b}$, so we only consider this helicity combination in the following discussion. The total $b\bar{b}g$ cross section is calculated for all three partons in the angular range $|\cos \theta| < 0.7$, and the infrared singularity is avoided by imposing a cut $E_g > 1$ GeV. Figure 5 shows the distribution in gluon energy for the massive and massless cases. The very different behavior of the two cross sections at small E_g is apparent. The effect of the non-zero b -quark mass is also evident near the upper kinematic limit, $E_g = \sqrt{s}/2$.³ The two distributions are similar when $m_b \ll E_g \ll \sqrt{s}$. The effect of the infrared singularity becomes weaker at higher collision energy. This is illustrated by the second set of curves for $\sqrt{s} = 500$ GeV in Fig. 5.

In the massless case the gluon prefers to be hard because, as we have seen, the matrix

³In practice, the behaviour close to the upper kinematic limit will be strongly modified by higher-order corrections.

element suppresses soft gluons; for $E_g \ll \sqrt{s}$ the cross section behaves as

$$\frac{d\sigma}{dE_g}(\gamma\gamma \rightarrow q\bar{q}g, J_z = 0, m_q = 0) \sim \alpha^2 \alpha_s \frac{E_g^3}{s^3} [\dots]. \quad (16)$$

In the massive case, the matrix element has an infrared singularity in the limit $k \rightarrow 0$. In this limit, the matrix element factorizes into a ‘probability of soft gluon emission’ times the lowest order matrix element,

$$\lim_{k \rightarrow 0} |\mathcal{M}_{\lambda_1, \lambda_2}(\gamma\gamma \rightarrow q\bar{q}g)|^2 \rightarrow \mathcal{S}(p, \bar{p}; k) |\mathcal{M}_{\lambda_1, \lambda_2}(\gamma\gamma \rightarrow q\bar{q})|^2, \quad (17)$$

where

$$\mathcal{S}(p, \bar{p}; k) = g_s^2 C_F \left[\frac{2 p \cdot \bar{p}}{(p \cdot k)(\bar{p} \cdot k)} - \frac{m_q^2}{(p \cdot k)^2} - \frac{m_q^2}{(\bar{p} \cdot k)^2} \right], \quad (18)$$

$$|\mathcal{M}_{\lambda_1, \lambda_2}(\gamma\gamma \rightarrow q\bar{q})|^2 = \frac{6e^4 Q_q^4}{t^2 u^2} [2m_q^2 s^2 (s - 2m_q^2) + (1 - \lambda_1 \lambda_2)(t^2 + u^2)(tu - 2m_q^2 s)], \quad (19)$$

and $s = 2 k_1 \cdot k_2$, $t = -2 k_1 \cdot p$, $u = -2 k_1 \cdot \bar{p}$. In the infrared limit and with small quark masses, i.e. $E_g \ll m_q \ll \sqrt{s}$, the cross section behaves as

$$\frac{d\sigma}{dE_g}(\gamma\gamma \rightarrow q\bar{q}g, J_z = 0, m_q \neq 0) \sim \alpha^2 \alpha_s \frac{m_q^2}{s^2 E_g} [\dots]. \quad (20)$$

In the total cross section, this infrared singularity is cancelled by one-loop virtual-gluon corrections to the lowest order $\gamma\gamma \rightarrow q\bar{q}$ process. The net effect is a finite $\mathcal{O}(\alpha_s)$ correction,

$$\sigma_{J_z=0}(\gamma\gamma \rightarrow q\bar{q}g) = \sigma_{J_z=0}(\gamma\gamma \rightarrow q\bar{q}) [1 + \alpha_s C + \mathcal{O}(\alpha_s^2)], \quad (21)$$

with C a known coefficient, see for example [18]. To avoid spurious large contributions from the soft-gluon region, in what follows we will impose a cut $E_g > E_{\min} = \sqrt{s}/10$. None of our results depend sensitively on this parameter. We should mention also that the same infrared problems are encountered in the next-to-leading order Higgs decay process $H \rightarrow b\bar{b}g$, where the addition of virtual-gluon corrections lead to a finite $\mathcal{O}(\alpha_s)$ correction to the leading-order decay width.

3 Experimental Considerations

The $J_z = 0, \gamma\gamma \rightarrow q\bar{q}g$ cross section, even for small values of y_{cut} , is a few per cent of the $J_z = \pm 2, \gamma\gamma \rightarrow q\bar{q}$ cross section. This cross section for bottom and charm quarks, in the approximation of Eq. (7) with $y_{\text{cut}} = 0.02$, along with the non-radiative backgrounds is shown in Fig. 6.

In a photon linear collider, it is possible to achieve a $\frac{J_z=0}{J_z=\pm 2}$ ratio of 20–50, so in order to bring the *rates* for the radiative processes down well below that of the non-radiative

processes, it is necessary to find cuts which further reduce the radiative backgrounds by a factor of about 5–10, without seriously degrading the $H \rightarrow b\bar{b}$ signal. In order to explore whether this is possible, we have employed a Monte Carlo integration of the radiative cross section with massive quarks which includes fragmentation and hadronization (via JETSET 6.3 [19]) and a simple detector simulation. The detector simulation is a gaussian smearing of the final state four-momenta by resolutions typical of detectors considered for a Next Linear Collider, such as the JLC detector [20]. Vertexing, tracking, and calorimetry are all simulated, but particle identification is not.

We assume a $\gamma\gamma$ invariant mass of 100 GeV and require that the thrust axis satisfy $|\cos\theta| < 0.7$. Imposing a y_{cut} of 0.02 to define two-jet events, the values of the relevant cross sections are as follows:

$$\begin{aligned}\sigma_{J_z=0}(\gamma\gamma \rightarrow H \rightarrow b\bar{b} \rightarrow 2 \text{ jets}) &= 0.86 \text{ pb}, \\ \sigma_{J_z=\pm 2}(\gamma\gamma \rightarrow b\bar{b} \rightarrow 2 \text{ jets}) &= 2.21 \text{ pb}, \\ \sigma_{J_z=\pm 2}(\gamma\gamma \rightarrow c\bar{c} \rightarrow 2 \text{ jets}) &= 35.6 \text{ pb}, \\ \sigma_{J_z=0}(\gamma\gamma \rightarrow b\bar{b}g \rightarrow 2 \text{ jets}) &= 0.035 \text{ pb}, \\ \sigma_{J_z=0}(\gamma\gamma \rightarrow c\bar{c}g \rightarrow 2 \text{ jets}) &= 0.87 \text{ pb}.\end{aligned}\tag{22}$$

3.1 Event Shape and Jet Width Cuts

Although a y_{cut} of 0.02 tends to select very two-jet-like events, the $q\bar{q}g$ events still tend to be more spherical than the $q\bar{q}$ events, as shown in Fig. 7(a). A cut on event sphericity then further reduces the radiative cross section without greatly diminishing the $q\bar{q}$ rate. The efficiency as a function of sphericity cut is shown in Fig. 7(b).

Recall that the dominant contribution to the radiative cross section comes from the virtual Compton configuration, in which the final state can be described as a hard quark back-to-back with a gluon and a soft quark nearly at rest. As gluon jets tend to be broader than quark jets, a cut on the width of the final state jets preferentially cuts the radiative final state over the non-radiative final state. Specifically, we cut on the opening half-angle of the cone that contains 90% of the jet energy. Fig. 8(a) shows the distribution of this angle for both radiative and non-radiative processes. The efficiency as a function of $\theta_{90\%}$ is plotted in Fig. 8(b).

Choosing a sphericity cut of 0.02 and a $\theta_{90\%}$ cut of 20° results in the following efficiencies:

$$\begin{aligned}\epsilon(b\bar{b}) &= 91.2\%, & \epsilon(b\bar{b}g) &= 15.1\%, \\ \epsilon(c\bar{c}) &= 94.4\%, & \epsilon(c\bar{c}g) &= 34.0\%.\end{aligned}\tag{23}$$

3.2 Vertex Cuts

One might think that since the $b\bar{b}g$ final state—in the dominant kinematic configuration—contains one fast and one slow b quark that the vertex structure might differ greatly from

a $b\bar{b}$ final state with two fast quarks. In practice, it turns out that the vertex structure is similar for these two final states. The B hadrons from the slow b quark tend to be ‘pulled’ into the gluon jet and do give rise to displaced vertices in the gluon jet. Vertexing therefore is not a powerful discriminant between the radiative and non-radiative processes. Such a displacement of B hadrons towards the gluon side is a consequence of the well-known ‘string’ [21] or ‘drag’ [22] effect. It reflects the fact that particle production is governed by the collective action of color-connected partons, in this case the spectator quark and the outgoing gluon. Note also that because of the difference in the color topology of the underlying subprocesses, the structure of particle flow in the $q\bar{q}$ and Compton-regime $q\bar{q}g$ events has some distinct differences (see for example Ref. [23]) which, in principle, could be exploited to further discriminate between these types of events.

Distinguishing charm from bottom, however, will rely crucially on vertexing, both for the radiative and non-radiative processes. Although it is not our intention here to exhaustively examine this issue, the factor of 16 amplification of the charm cross sections over the bottom cross sections necessitates at least some discussion.

As B hadrons are long-lived, they tend to travel a finite distance before decaying, so that their decay products form displaced vertices which are measureable with modern vertex detectors. The same is true of charmed hadrons, but they tend to travel less far than B 's and have fewer tracks with displaced vertices. Vertexing is therefore a very useful tool both in separating light (u, d, s) from heavy (c, b) quark jets and in separating b 's from c 's.

Rather than reconstructing each decay vertex from the charged tracks in an event, it is sufficient to find the impact parameter (distance of closest approach, either in 3 dimensions or in the x - y plane) for each track. Modern vertex detectors are capable of impact parameter resolutions of $\sim 30 \mu\text{m}$. Requiring each event to have, say, 4 or 5 tracks with high ($> 4\sigma$) impact parameter (not including tracks which form K_S 's or Λ 's) results in the following efficiencies.

| process | 2-D | | 3-D | |
|-------------|----------|----------|----------|----------|
| | 4 tracks | 5 tracks | 4 tracks | 5 tracks |
| bb | 57% | 37% | 77% | 61% |
| $b\bar{b}g$ | 54% | 37% | 72% | 59% |
| $c\bar{c}$ | 3.7% | 0.8% | 5.9% | 1.6% |
| $c\bar{c}g$ | 4.4% | 1.0% | 7.4% | 2.0% |

Applying a sphericity cut of 0.02, a jet width cut of 20° , and requiring 5 tracks with high 3-D impact parameter then results in the following production cross sections:

$$\begin{aligned}
 \sigma_{J_z=0}(\gamma\gamma \rightarrow H \rightarrow b\bar{b} \rightarrow 2 \text{ jets}) &= 0.48 \text{ pb}, \\
 \sigma_{J_z=\pm 2}(\gamma\gamma \rightarrow b\bar{b} \rightarrow 2 \text{ jets}) &= 1.2 \text{ pb}, \\
 \sigma_{J_z=\pm 2}(\gamma\gamma \rightarrow c\bar{c} \rightarrow 2 \text{ jets}) &= 0.54 \text{ pb}, \\
 \sigma_{J_z=0}(\gamma\gamma \rightarrow b\bar{b}g \rightarrow 2 \text{ jets}) &= 0.0031 \text{ pb}, \\
 \sigma_{J_z=0}(\gamma\gamma \rightarrow c\bar{c}g \rightarrow 2 \text{ jets}) &= 0.0059 \text{ pb}.
 \end{aligned} \tag{24}$$

4 Summary and Conclusions

The identification of the intermediate-mass Higgs boson via the process $\gamma\gamma \rightarrow H \rightarrow b\bar{b}$ will be one of the most important goals of a future photon linear collider. Potentially important backgrounds from the continuum $\gamma\gamma \rightarrow c\bar{c}, b\bar{b}$ leading-order processes can be suppressed by a factor m_q^2/s by using polarized photon beams in the $J_z = 0$ initial-state configuration. In this paper we have pointed out that the same m_q^2/s suppressions do not apply to the radiative processes $\gamma\gamma \rightarrow c\bar{c}g, b\bar{b}g$. These processes can mimic the two-jet topology of the Higgs signal when two of the three partons are collinear, or when one of the partons is soft or directed down the beam pipe. Our detailed numerical calculations of the various two-jet cross sections, summarized in Eq. (22), show that these radiative processes do indeed provide the dominant background in the $J_z = 0$ channel. Particularly problematic is the $c\bar{c}g$ background which, because of the quark charge, is much larger than the corresponding b -quark process. For our choice of kinematic cuts and for a $\gamma\gamma$ collision energy of 100 GeV, the $\gamma\gamma \rightarrow c\bar{c}g \rightarrow 2$ jets background is comparable to the Higgs signal. In order to try to reduce this background further, we have studied the effect of additional event shape, jet width and vertex cuts. The results, described in Section 3 and summarized in Eq. (24), indicate that further improvements in the signal to background ratio can indeed be achieved. In particular, a modern vertex detector should be capable of achieving the necessary rejection of c -quark events while remaining reasonably efficient for the signal b -quark events.

Acknowledgements

We would like to acknowledge valuable discussions with Gary Greenbaum, Mike Strauss, and Mike Hildreth. This work was supported in part by the United Kingdom Science and Engineering Research Council, by the United States Department of Energy under Grants Nos. DOE-FG-91ER40618 and DE-FG03-91ER40674, and by Texas National Research Laboratory Grant No. RGFY93-330.

References

- [1] I.F. Ginzburg *et al.*, Nucl. Inst. Meth. **205**, 47 (1983); *ibid.* **219**, 5 (1984).
- [2] V.I. Telnov, Nucl. Inst. Meth. **A294**, 72 (1990).
- [3] D.L. Borden, D.A. Bauer, and D.O. Caldwell, preprints SLAC-PUB-5715 (1992) and UCSB-HEP-92-01 (1992).
- [4] F.R. Arutyunian and V.A. Tumanian, Phys. Lett. **4**, 176 (1963).
- [5] R.H. Milburn, Phys. Rev. Lett. **10**, 75 (1963).
- [6] J.F. Gunion and H.E. Haber, Phys. Rev. **D48**, 5109 (1993).

- [7] D.L. Borden, D.A. Bauer, and D.O. Caldwell, Phys. Rev. **D48**, 4018 (1993).
- [8] J.F. Gunion, H.E. Haber, G. Kane, and S. Dawson, *The Higgs Hunters Guide, Frontiers in Physics Series* Vol. 80 (Addison-Wesley, Redwood City, CA, 1990).
- [9] H. Konig, Phys. Rev. **D45**, 1575 (1992).
- [10] K.A. Ispiryan, I.A. Nagorskaya, A.G. Oganesyan and V.A. Khoze, Yad. Fiz. **11**, 1278 (1970) [Sov. J. Nucl. Phys. **11**, 712 (1970)];
- [11] R. Gastmans and T.T. Wu, *The Ubiquitous Photon: Helicity Method for QED and QCD* (Oxford University Press, Oxford, 1990), p. 479.
- [12] F.E. Low, Phys. Rev. **110**, 974 (1958).
- [13] T.H. Burnett and N.M. Kroll, Phys. Rev. Lett. **20**, 86 (1968).
- [14] JADE Collaboration, W. Bartel *et al.*, Z. Phys. **C26**, 93 (1984).
- [15] V.N. Baier, V.S. Fadin, and V.A. Khoze, Nucl. Phys. **B65**, 381 (1973).
- [16] R. Kleiss and W.J. Stirling, Phys. Lett. **B179**, 159 (1986).
- [17] V. Barger, A.L. Stange, and R.J.N. Phillips, Phys. Rev. **D44**, 1987 (1991).
- [18] M. Drees, M. Krämer, J. Zunft, and P.M. Zerwas, Phys. Lett. **B306**, 371 (1993); J.H. Kühn, E. Mirkes, and J. Steegborn, Z. Phys. **C57**, 615 (1993).
- [19] T. Sjöstrand, Comput. Phys. Commun. **27**, 243 (1982); T. Sjöstrand and M. Bengtsson, *ibid.* **43**, 367 (1987).
- [20] KEK Report 92-16 (1992).
- [21] B. Andersson, G. Gustafson, and T. Sjöstrand, Phys. Lett. **B94**, 211 (1980).
- [22] Ya.I. Azimov, Yu.L. Dokshitzer, V.A. Khoze, and S.I. Troyan, Phys. Lett. **165B**, 147 (1985).
- [23] Yu.L. Dokshitzer, V.A. Khoze, A.H. Mueller, and S.I. Troyan, *Basics of Perturbative QCD*, Editions Frontieres, 1991.

Figures

1. Cross section for $\gamma\gamma \rightarrow H \rightarrow b\bar{b}$ as a function of the Higgs mass. A value of 0.2 $\text{fb}^{-1}/\text{GeV}$ has been taken for dL/dW .
2. Cross sections for $\gamma\gamma \rightarrow b\bar{b}$ and $\gamma\gamma \rightarrow c\bar{c}$ in polarized collisions. A cut of $|\cos\theta| < 0.7$ has been applied. For comparison, the Higgs boson signal has been superimposed, with the normalization as described in the text.
3. Examples of how the $q\bar{q}g$ final state can appear as two jets: a) two partons are collinear, b) one of the partons is soft or directed down the beam pipe. The solid and wavy lines represent quarks and gluons, respectively.
4. Diagram of $x-\bar{x}$ phase space showing the two- and three-jet event regions.
5. Distribution of the gluon energy in the process $\gamma\gamma \rightarrow b\bar{b}g$ for massless and massive ($m_b = 4.5$ GeV) b -quarks for center-of-mass energies $\sqrt{s} = 200$ and 500 GeV.
6. Cross sections for $\gamma\gamma \rightarrow b\bar{b}, c\bar{c}$ and $\gamma\gamma \rightarrow b\bar{b}g, c\bar{c}g$. The approximaton of Eq. (7) is used for the radiative cross sections.
7. a) Sphericity distribution of $b\bar{b}$ and $b\bar{b}g$ events. b) Efficiency as a function of sphericity cut for $b\bar{b}$ and $b\bar{b}g$ events.
8. a) Distribution of opening half-angles of cones containing 90% of the jet energy for $b\bar{b}$ and $b\bar{b}g$ events; a sphericity cut of 0.02 is included. b) Efficiency as a function of cut on $\theta_{90\%}$ for $b\bar{b}$ and $b\bar{b}g$ events.

This figure "fig1-1.png" is available in "png" format from:

<http://arXiv.org/ps/hep-ph/9405401v2>

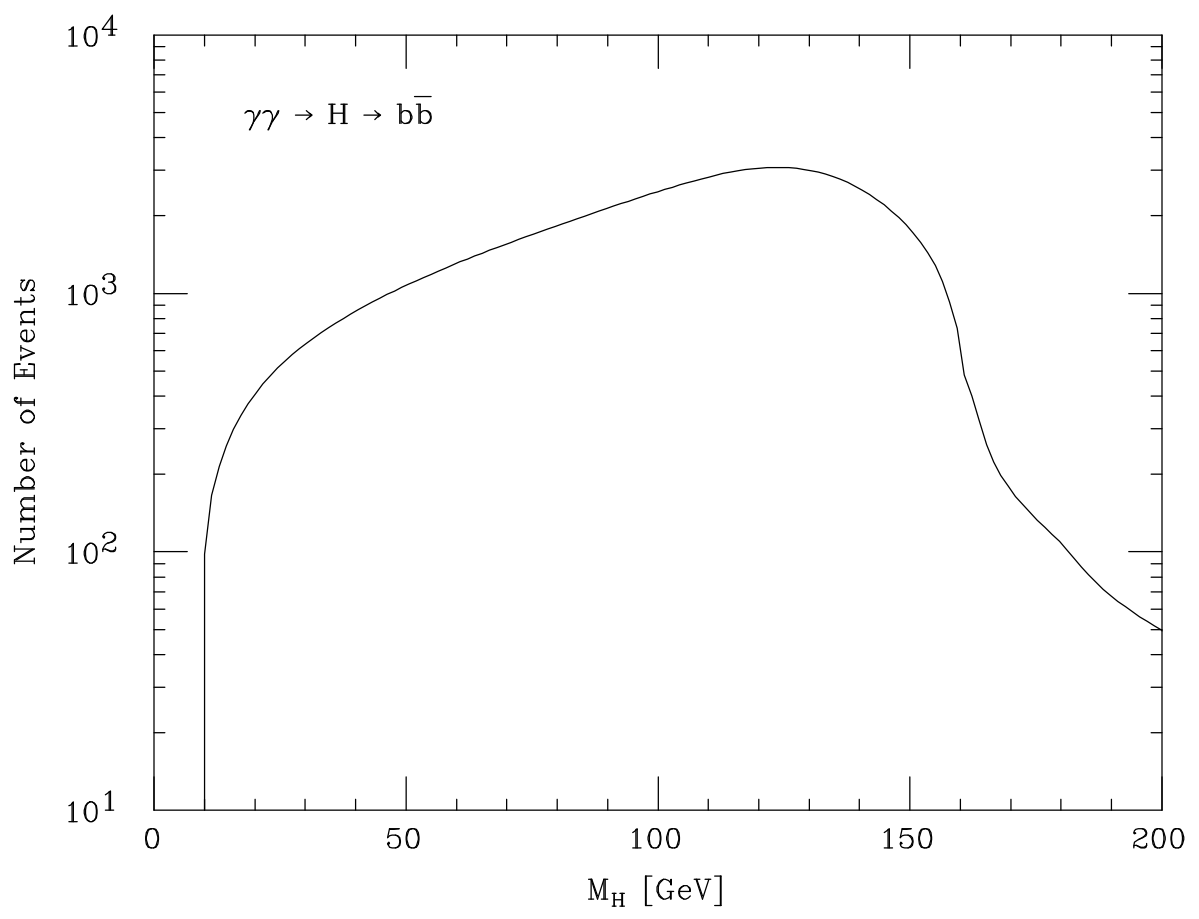


Figure 1

This figure "fig2-1.png" is available in "png" format from:

<http://arXiv.org/ps/hep-ph/9405401v2>

This figure "fig3-1.png" is available in "png" format from:

<http://arXiv.org/ps/hep-ph/9405401v2>

This figure "fig4-1.png" is available in "png" format from:

<http://arXiv.org/ps/hep-ph/9405401v2>

This figure "fig1-2.png" is available in "png" format from:

<http://arXiv.org/ps/hep-ph/9405401v2>

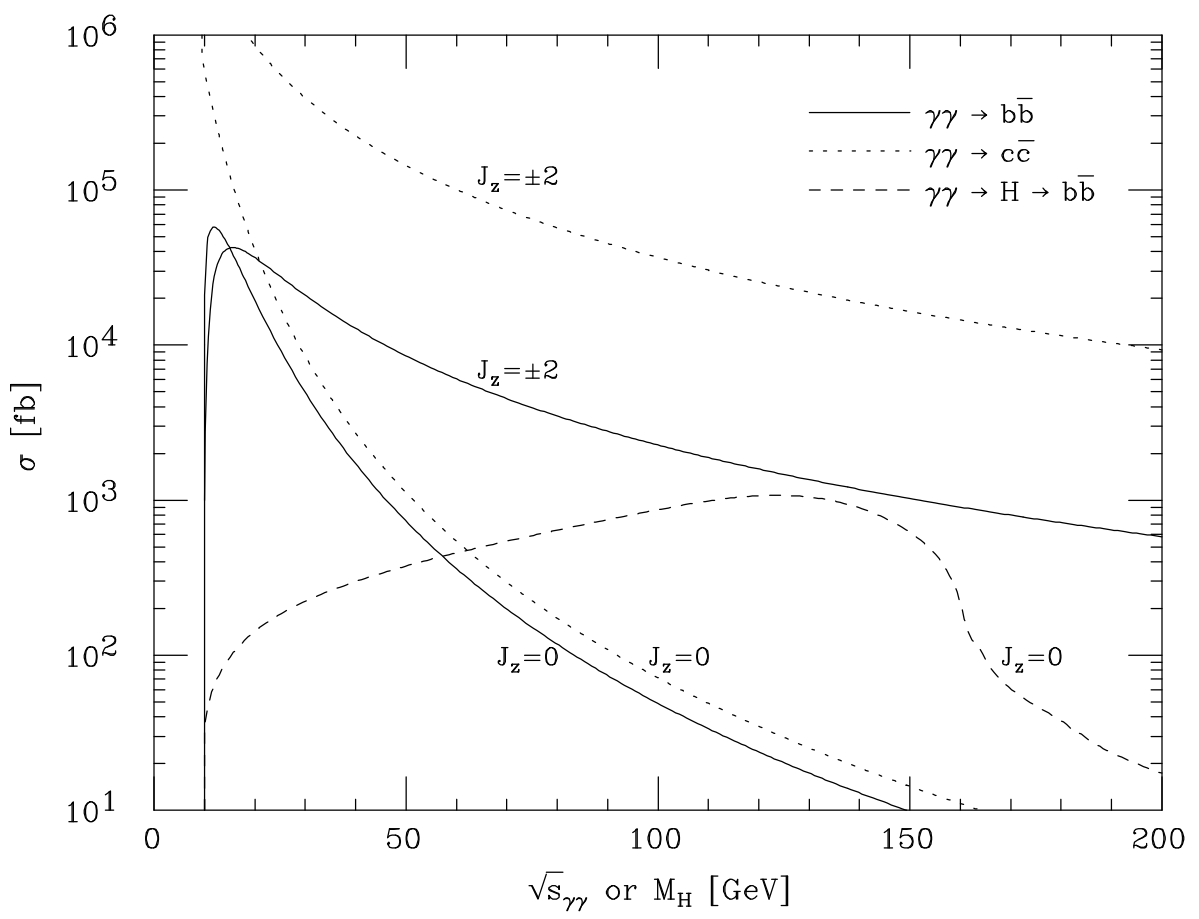


Figure 2

This figure "fig4-2.png" is available in "png" format from:

<http://arXiv.org/ps/hep-ph/9405401v2>

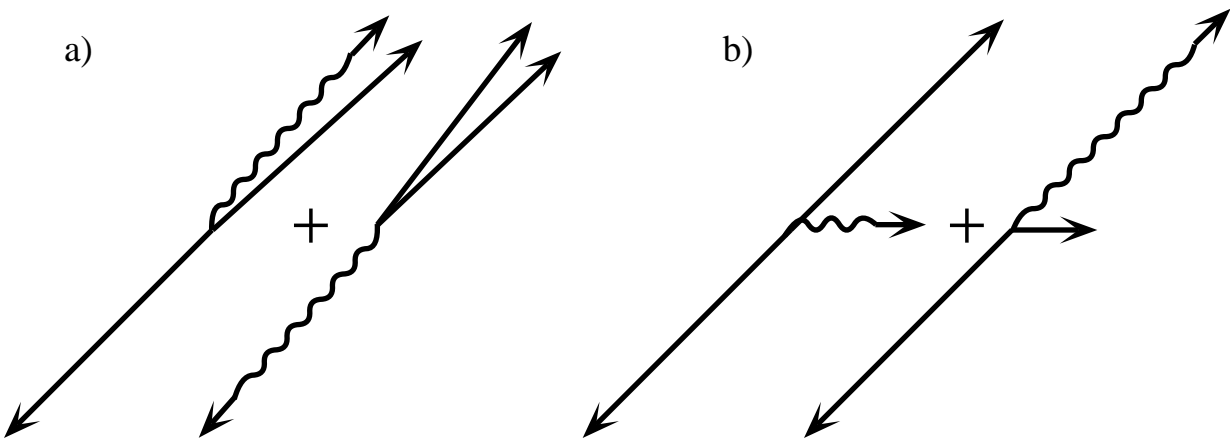


Figure 3

This figure "fig4-3.png" is available in "png" format from:

<http://arXiv.org/ps/hep-ph/9405401v2>

This figure "fig4-4.png" is available in "png" format from:

<http://arXiv.org/ps/hep-ph/9405401v2>

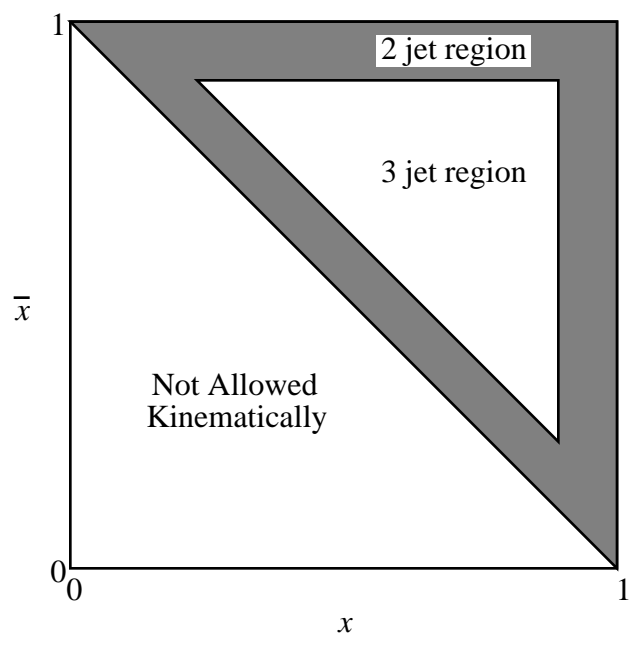


Figure 4

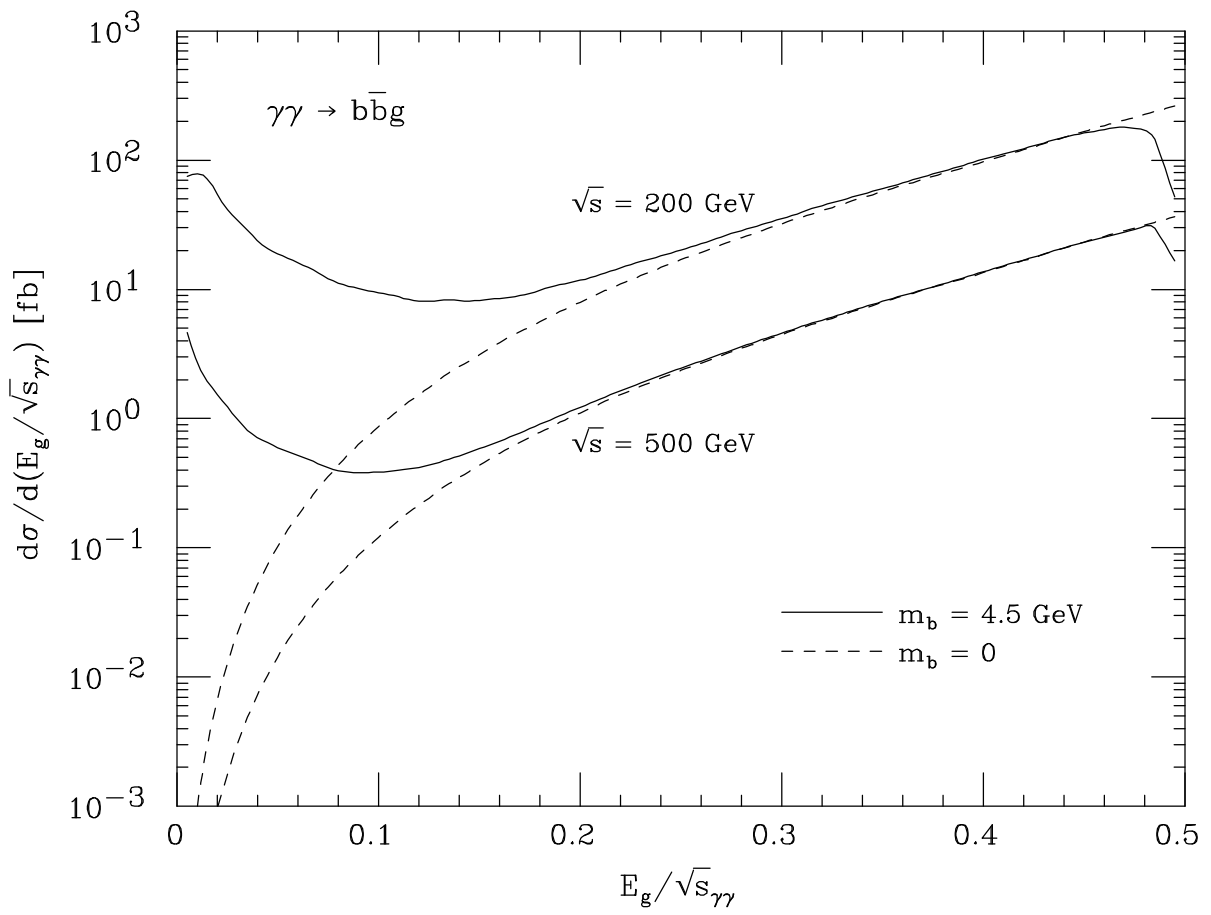


Figure 5

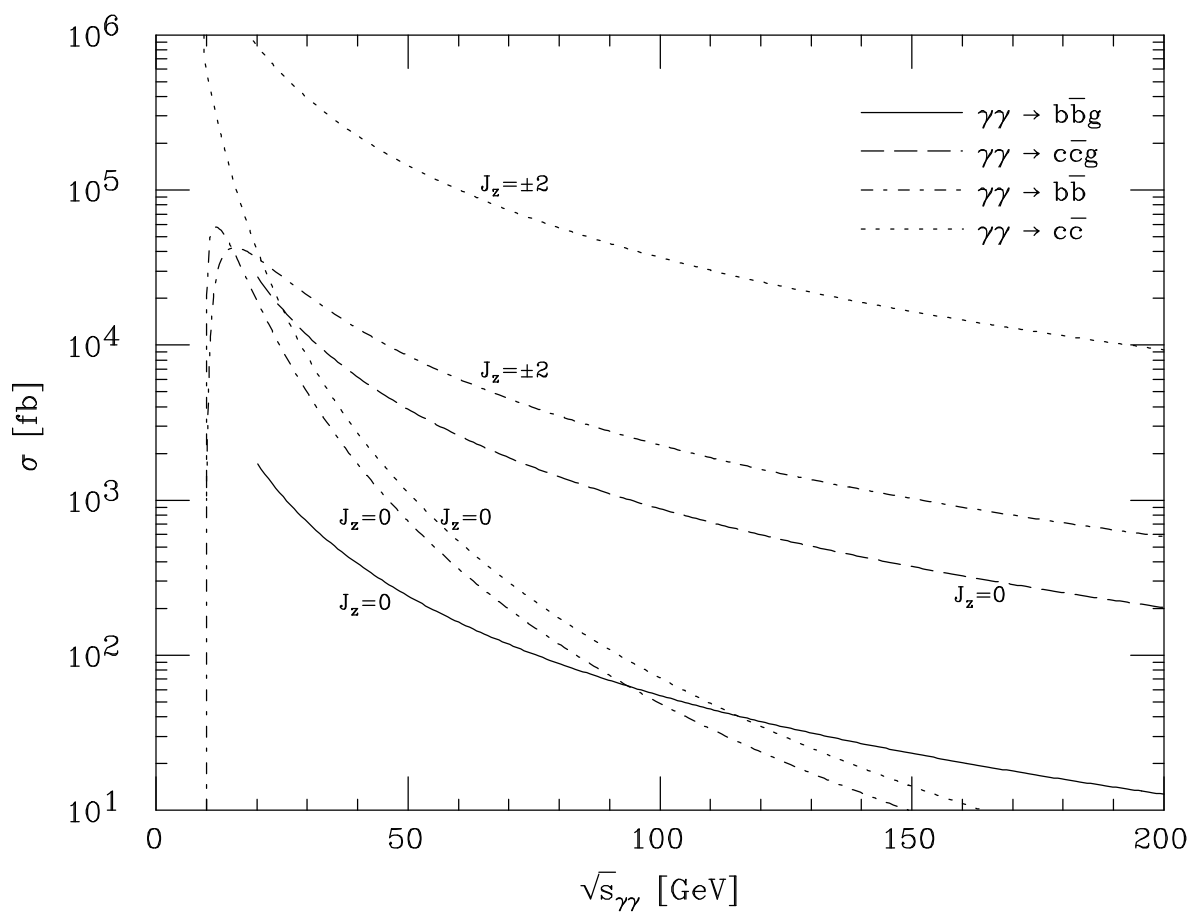


Figure 6

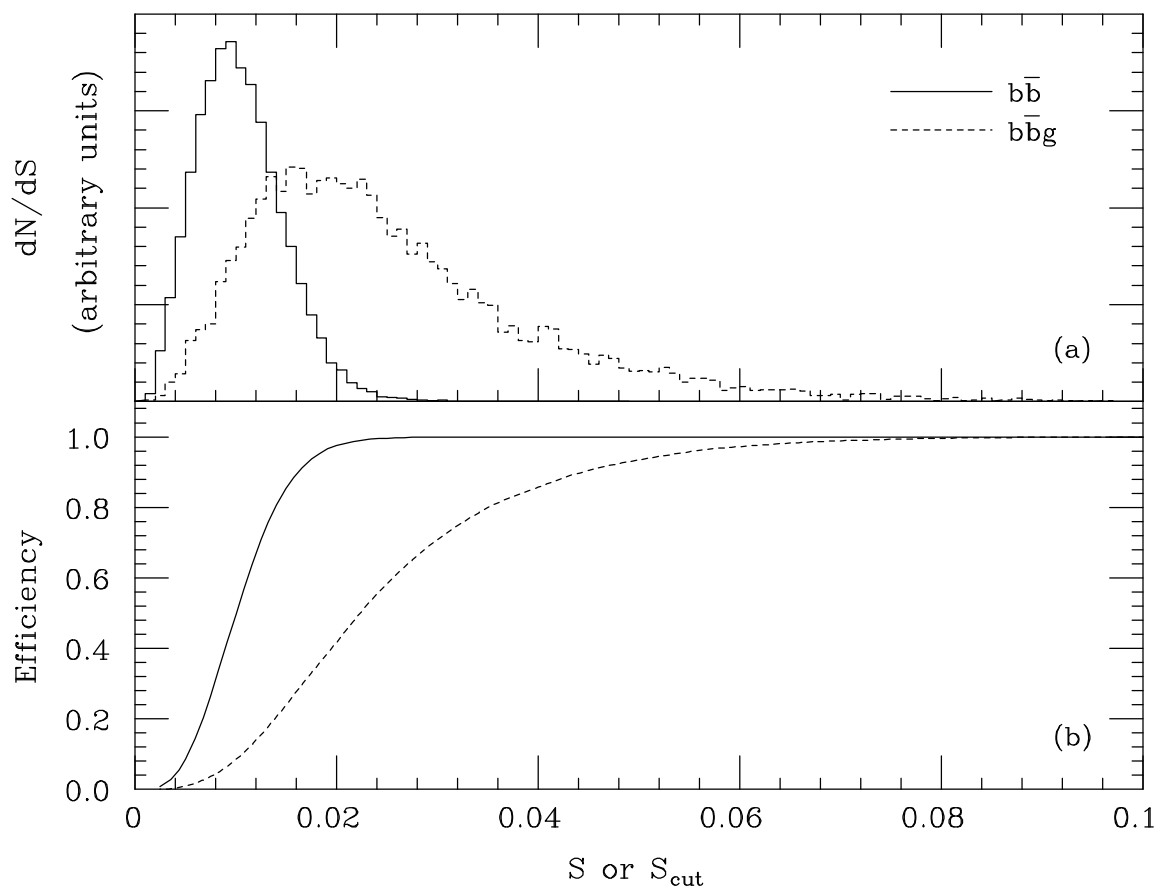


Figure 7

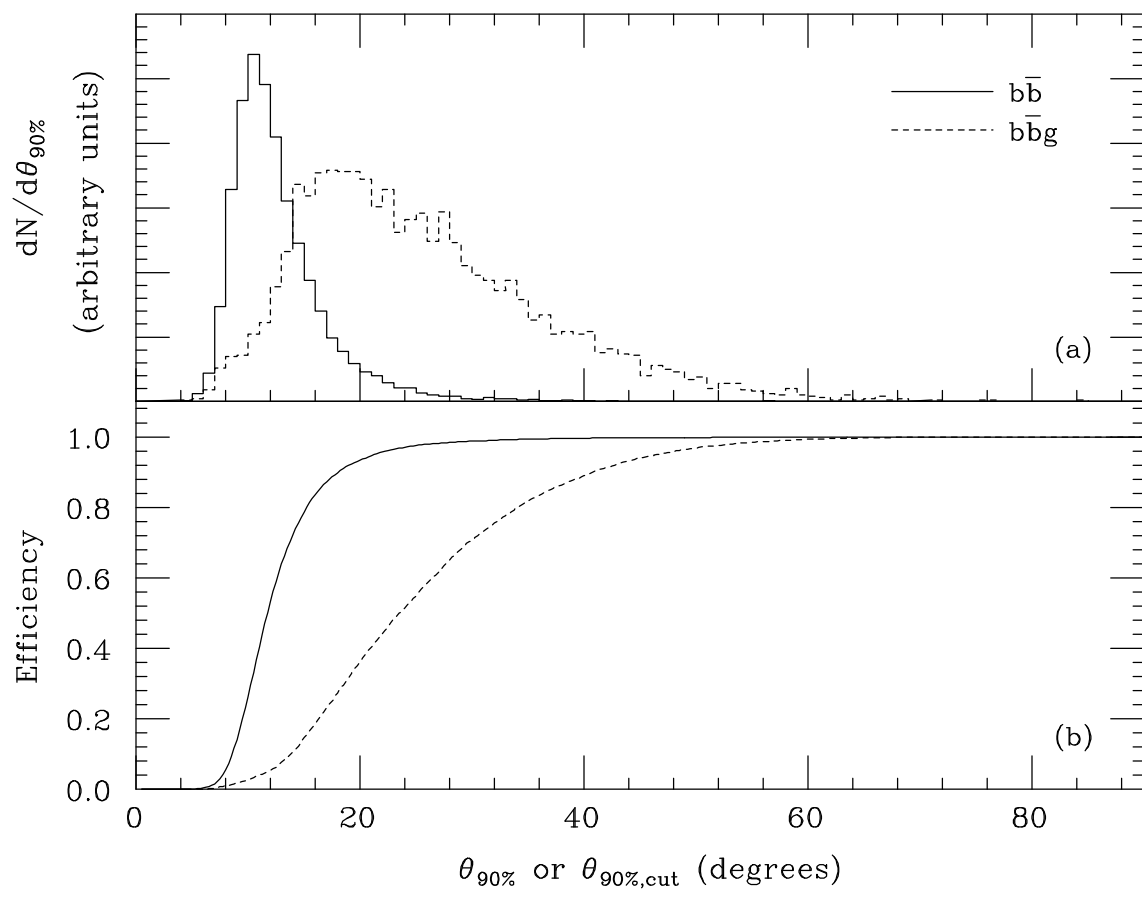


Figure 8